GEOPERSIA

Accepted Manuscript

Scanning X-ray Fluorescence Microanalysis of Phosphorites from the Jeirud Formation, Iran

Mahboobeh Jamshidibadr, Seyed Javad Moghaddasi, David Richard Lentz

DOI: 10.22059/geope.2026.409093.648858

Receive Date: 01 January 2026
Revise Date: 23 February 2026
Accept Date: 03 May 2026

Scanning X-ray Fluorescence Microanalysis of Phosphorites from the Jeirud Formation, Iran

Mahboobeh Jamshidibadr [1], *, Seyed Javad Moghaddasi [1], David Richard Lentz [2]

[1] Department of Geology, Payame Noor University, Tehran, Iran
[2] Department of Earth Sciences, University of New Brunswick, Fredericton, New Brunswick E3B 5A3, Canada

Received: 01 January 2026, Revised: 23 February 2026, Accepted: 03 May 2026

Abstract
The phosphorite deposits of the Upper Devonian Jeirud Formation in the Central Alborz, Iran, represent a significant resource within the extensive Tethyan phosphate belt, interpreted as having precipitated in a shallow marine setting influenced by upwelling and anoxic bottom waters. This investigation utilizes high-resolution micro-X-ray fluorescence (μ-XRF) spectrometry to conduct a detailed, spatially resolved analysis of elemental distributions, paragenetic mineralogy, and multi-stage diagenetic pathways within these sedimentary rocks. Comprehensive elemental mapping definitively identifies fluorapatite as the predominant phosphate mineral, manifesting in two principal modes: (i) reworked, rounded to sub-rounded peloids and intraclasts, and (ii) microcrystalline cement. The μ-XRF data provide unequivocal evidence for a key diagenetic overprint involving the partial to complete oxidative replacement of primary phosphate phases by iron (oxyhydr)oxides. Concurrently, the technique facilitates the precise identification of accessory mineralogy, including euhedral pyrite (confirmed via strong Fe–S spatial correlation) and Ti-bearing phases such as rutile or titanite. Quantitative spot analyses reveal significant enrichment of rare earth elements (REEs) within the fluorapatite lattice. Critically, a robust linear correlation between quantitative μ-XRF-derived concentrations and conventional bulk ICP-OES data from paired samples validates the μ-XRF methodology as a highly accurate, reliable, and non-destructive alternative for quantitative geochemical characterization of phosphorites. The study establishes μ-XRF as a powerful tool for deciphering complex paragenetic sequences, elucidating primary sedimentary versus diagenetic textures, and reconstructing post-depositional alteration histories, thereby offering significant utility for both academic research and mineral resource evaluation of phosphate deposits.

Keywords: μ-XRF, Phosphorite, Jeirud Formation, Central Alborz, Iran.

Introduction

Sedimentary deposits constitute approximately 95% of the world's phosphate resources, with igneous types, typically associated with carbonatites and alkaline intrusions, making up the remaining 5% (Pufahl et al., 2003; Pufahl & Groat, 2016; Jasinski, 2016). Phosphorites are marine biochemical sedimentary rocks, generally containing about 18 wt% P_2O_5, and serve as the primary source for fertilizer production (Glenn et al., 1994). Typical phosphorites exhibit P_2O_5 contents of 15–20 wt% and uranium concentrations of 50–120 ppm (Boggs, 2009; Tzifas et al., 2014; Pufahl & Groat, 2016). These deposits predominantly form in warm climates at low paleolatitudes (<30°) within shallow marine settings characterized by high bioproductivity and low sedimentation rates (Banerjee et al., 2020). Globally, sedimentary phosphorites are found in over 80 countries, with ages ranging from the Paleoproterozoic to the Recent (Orris & Chernoff, 2004;

* Corresponding author e-mail: m_jamshidi@pnu.ac.ir

Abed, 2013).

Sedimentary phosphorites account for more than 75% of global phosphate production (Cook et al., 1990; Orris & Chernoff, 2004). Phosphate particles occur in various forms, including pellets, intraclasts, nodules, peloids, coated grains, coprolites, and vertebrate bone and tooth fragments. The Middle East hosts significant sedimentary phosphorite resources that developed progressively from the Paleocene to Eocene (Garnit et al., 2012, 2017; Kocsis et al., 2014, 2016; Kechiched et al., 2020). A small area of the eastern Mediterranean contains an estimated 20 billion tonnes of high-grade phosphate deposits, spanning Jordan, Palestine, northwestern Saudi Arabia, western Iraq, southeastern Syria, and southwestern Iran (Abed, 2013; Abed et al., 2016).

In Iran, most sedimentary phosphates belong to the Neo-Tethyan phosphorite province, which also encompasses major producing regions in North Africa, northern South America, and the Caribbean, with deposition linked to late Cretaceous to Eocene open-ocean–related settings (Notholt et al., 1989; Lucas & Prévôt-Lucas, 1995; Föllmi, 1996; Van Kauwenbergh, 2010; Jasinski, 2011; Abed, 2013). Deposition of phosphorites in the Tethyan realm was particularly significant during the late Cretaceous to Eocene (Lucas & Prévôt-Lucas, 1995).

Recently, (Hashempour et al., 2024) classified Iran's sedimentary phosphate deposits based on general geology, mineralization characteristics, ore controls, and tectonic setting into three main belts: (1) Alborz Magmatic Belt, (2) Central Iran, and (3) Zagros Fold-Thrust Belt. They proposed distinct formation periods linked to tectonic settings: (1) Neoproterozoic–Early Cambrian (Soltanieh Formation), (2) Ordovician–Silurian (Shirgesht, Mila, Seyahou formations), (3) Upper Devonian (Jeirud Formation), (4) Permian–Jurassic, and (5) Cretaceous–Eocene (Gurpi and Pabdeh formations). The Alborz Magmatic Belt and Zagros Fold-Thrust Belt are considered the most prospective regions for undiscovered sedimentary phosphorite deposits in Iran (Fig. 1).

The most Iranian sedimentary phosphorite deposits formed during opening and closure cycles of the Tethys Ocean, with primary depositional environments typically being shallow slope and shelf facies. The principal periods of sedimentary phosphate (SP-type) mineralization occurred during the Upper Devonian and the Cretaceous–Eocene. The economically most significant Iranian phosphorite deposits are hosted within the Upper Devonian Jeirud Formation (Hashempour et al., 2024).

This study applies high-precision micro-X-ray fluorescence (μ-XRF) spectrometry to characterize the Jeirud Formation phosphorites, focusing on fluorapatite and accessory minerals such as pyrite, iron oxides, titanite, and zircon. By generating high-resolution elemental distribution maps, we reconstruct the paragenetic sequence and diagenetic pathways, illustrating how oxidative alteration of primary phosphate to iron oxides and the formation of Ti-bearing phases (e.g., titanite) occurred within the formation. Furthermore, by quantifying rare earth element (REE) incorporation into the apatite lattice and interpreting depositional redox conditions from REE patterns and anomalies, we assess the performance of μ-XRF relative to conventional bulk methods (ICP-OES/MS) using identical sample suites. This comparative framework aims to establish μ-XRF as a non-destructive, reliable alternative for geochemical evaluation of phosphate deposits and to present a methodological approach that integrates microscale spatial information with quantitative geochemistry, enabling discrimination of elements hosted in distinct mineral phases and linking primary depositional conditions to subsequent diagenetic evolution.

Materials and Methods

Micro-XRF Analysis

Micro-X-ray fluorescence (μ-XRF) is a non-destructive analytical technique used for spatially resolved elemental characterization at the microscale. It involves irradiating a sample with a focused X-ray beam and measuring the emitted secondary (fluorescence) X-rays. The method

allows for the simultaneous detection and quantification of a wide range of elements (typically from Mg to U), making it invaluable in geology, materials science, and environmental studies. µ-XRF has been successfully applied to the geochemical study of sedimentary sequences and phosphorites (e.g., Daryin et al., 1991; Shanahan et al., 2008; Zilkey et al., 2024).

For this study, four polished thin sections of phosphate rock from the Jeirud Formation were analyzed using a µ-XRF instrument at the University of New Brunswick, Canada. The micro-XRF instrument used in this study (a Bruker M4 Tornado) has a sample chamber that allows for analysis either at atmospheric pressure or under vacuum. The analyses were conducted under a vacuum. Specifically, the instrument is equipped with a pressure-controlled diaphragm pump to achieve an oil-free vacuum, and all measurements were carried out at 20 mbar. X-rays were generated from an Rh tube operating at 30–50 kV and 300–400 µA (Flude et al., 2017). A static X-ray spot size of 20 µm was used to perform raster scans, producing multi-element distribution maps. Single- or multi-element maps, where pixel intensity corresponds to elemental concentration, were generated to visualize mineralogy and textures (see Flude et al., 2017 for analytical methods and Heidarian et al., 2021).

A key advantage of µ-XRF over electron-beam techniques is its deeper penetration (hundreds of micrometers in silicates), providing bulk compositional information without the need for conductive coating. While its spatial resolution for very fine features (<25 µm) is lower than that of an electron microprobe, µ-XRF is highly effective for mapping the distribution of phosphate and associated elements, identifying mineral phases, and characterizing assemblages at the thin-section scale.

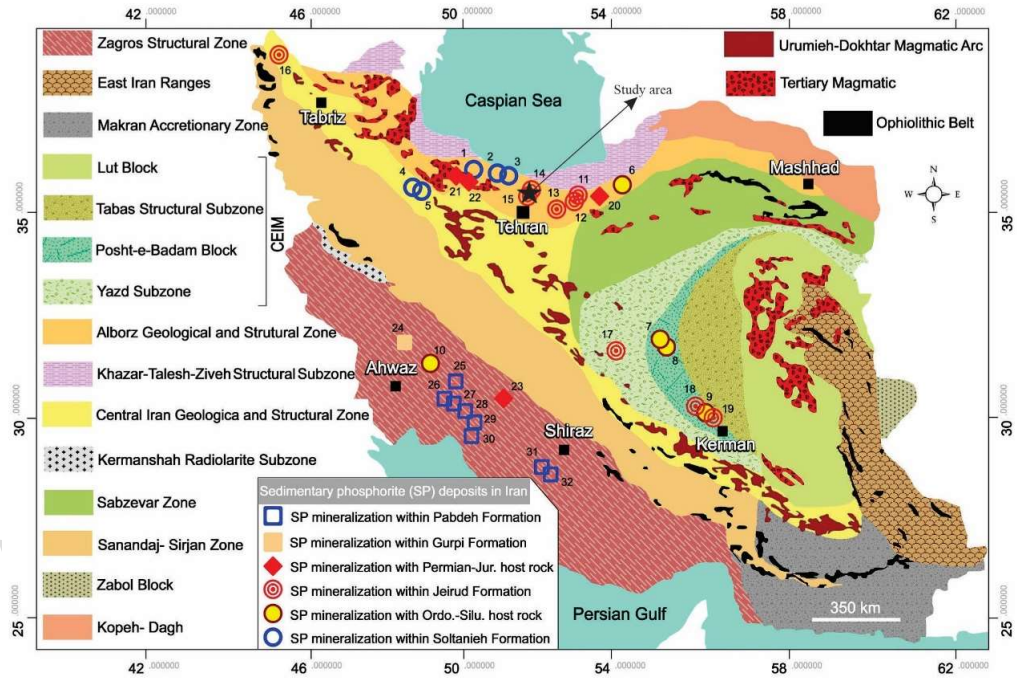

Figure 1. Distribution map of sedimentary phosphate (SP) deposits according to the age of host rocks within the main tectonic elements of Iran (modified after Hashempour et al., 2024). (Locations are approximate; tectonic map modified after Alavi, 1996; Aghanabati, 1998, 2004). CEIM: Central-East Iranian Microcontinent. Numbered deposits: 1: Dalir; 2: Valiabad; 3: Firoozabad; 4: Seyed-Kandi; 5: Takab-Shahindezh; 6: Shahmirzad; 7: Kalmard; 8: Rahdar; 9: Dahuieh; 10: Seyahou Formation; 11: Paghaleh; 12: Gaduk; 13: Firuzkuh; 14: Jeirud; 15: Meygun; 16: Mako; 17: Darrehbid; 18: Sarashk; 19: Hutk; 20: Abkhory; 21: Talegan; 22: Hosseinabad; 23: Faragan Mountain; 24: Gurpi Formation; 25: Kuh-Sefid; 26: Kuh-Rish; 27: Dehdasht; 28: Sheikh-Habil; 29: Kuh-e-Lar; 30: Doghonbadan; 31: Parsa; 32: Farrashband

Integration with Prior Geochemical Data

The μ-XRF results were interpreted in conjunction with previously published bulk geochemical data from the same rock suite (Moghaddasi, 2017). That reference dataset includes trace element concentrations determined by inductively coupled plasma optical emission spectrometry (ICP-OES; Varian 735 Radial) and rare earth element (REE) concentrations quantified by inductively coupled plasma mass spectrometry (ICP-MS; Agilent 4500) at LabWest Laboratories, Australia. This integration allows for the validation of μ-XRF-derived elemental patterns, attribution of bulk chemical signatures to specific host minerals (e.g., apatite), and distinction between elements within the phosphate matrix and those in rare accessory phases.

Geological Setting

The study area is located approximately 45 km north of Tehran, within the central Alborz Mountain range (geographic coordinates ~51°30′E, 36°00′N; see Figs. 1 & 2). The sampled rocks belong to the Upper Devonian Jeirud Formation, a major phosphate-bearing unit within the Ordovician to Early Carboniferous succession of the Alborz.

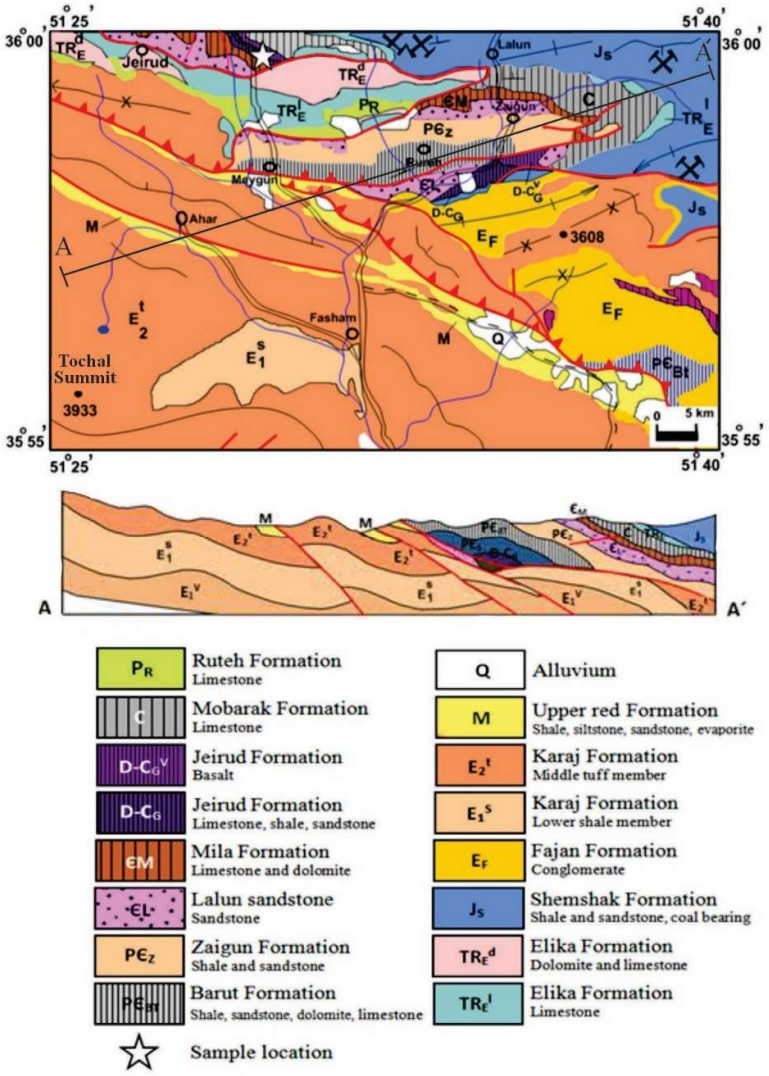

Figure 2. Geological map of the Meygun area north of Tehran, showing outcrops of the Jeirud Formation and the sampling location (modified from Haghipour et al., 1986)

In the central Alborz, the Jeirud Formation is widely interpreted to represent deposition in a nearshore to proximal shelf environment (Assereto, 1966; Ernst & Mohammadi, 2009). It comprises a mixed siliciclastic-carbonate sequence, with intercalated volcanic material, reflecting repeated transgressions and regressions along the northern margin of Gondwana (Wendt et al., 2005; Ghavidel-Syooki, 1995). The formation unconformably overlies the Middle Cambrian to Early Ordovician Mila Formation, with a significant stratigraphic hiatus attributed to Caledonian tectonic activity, and is conformably overlain by the Mobarak Formation (Carboniferous) dolomites and limestones.

The Jeirud Formation in the region is subdivided into four units (A–D), with Unit D not observed in the immediate study area (Assereto, 1963, 1966). The economically important phosphate horizons are hosted within Unit A. This unit begins with prograding sandstone overlying an erosional surface on the Mila Formation, followed by a brachiopod-rich limestone containing phosphatic clasts. This is overlain by approximately 30 m of pelitic, black fissile shale that hosts multiple phosphatic sandstone beds.

These phosphate beds are typically subdivided into a lower low-grade bed, a middle high-grade bed, and an upper low-grade bed, each 0.4–3 m thick. Unit A is capped by about 70 m of dark, dolomitic, brachiopod-rich limestones, succeeded by 100–140 m of basaltic lava flows (Avini, 1987). The stratigraphic positions of the phosphate samples collected from the Shemshak Valley are illustrated in Fig. 3.

Mineralogy

Petrographic analysis of the Jeirud Formation phosphorites, sampled from a basal 67-meter sequence containing at least 27 distinct phosphate-rich horizons, reveals a paragenetic sequence dominated by authigenic and biogenic phosphate minerals within a mixed siliciclastic-carbonate matrix (Namdmalian et al., 1998). The P_2O_5 content within these horizons is highly variable, ranging from ~1% to over 30% (Namdmalian et al., 1998; Moghaddasi, 2017).

The primary phosphate phase is collophane, a cryptocrystalline to microcrystalline variety of fluorapatite [$Ca_5(PO_4)_3F$]. It occurs in two principal modes: (1) as abundant, reworked rounded to sub-rounded peloids and intraclasts, and (2) as pervasive, authigenic microcrystalline cement binding the detrital framework (Figs. 4a–d). The peloids, ranging from tens to several hundred micrometers in diameter, frequently display diffuse margins and partial replacement by iron oxides, indicating post-depositional oxidative alteration (Fig. 5a, b). Under plane-polarized light, the isotropic collophane cement exhibits a characteristic brownish tint, consistent with its cryptocrystalline nature and common incorporation of organic matter. Elongated apatite grains suggest a biogenic origin, possibly representing reworked skeletal fragments or, as noted by (Namdmalian et al., 1998), vertebrate bone material (Fig. 5c).

The siliciclastic fraction (15–40% of the sandy phosphorites) is dominated by detrital quartz (Fig. 5d), occurring as well-rounded, silt- to sand-sized grains within the phosphatic matrix (Figs. 4a–d). These grains often show pressure dissolution contacts with adjacent phosphate peloids, indicating significant mechanical compaction prior to or during phosphate cementation.

Carbonate minerals, primarily calcite with subordinate dolomite, occur chiefly as pore-filling sparry cement post-dating phosphate formation (Figs. 5b, d). Their abundance is variable; in well-sorted, grain-supported phosphorites, carbonate cement is often minimal (<5%). Where present (5–20%), it occludes residual porosity and locally replaces phosphate grain margins, reflecting a later diagenetic phase under more alkaline conditions.

Iron-bearing phases constitute an important accessory assemblage (2–8% by volume). Euhedral to subhedral pyrite [FeS_2] is disseminated throughout the phosphate matrix as isolated

crystals and small aggregates (Fig. 5b), suggesting reducing, sulfidic conditions during early diagenesis. In oxidized zones, pyrite is partially to completely replaced by iron oxides/hydroxides (e.g., goethite, hematite), which stain the groundmass and form irregular patches along fractures (Figs. 6a, b).

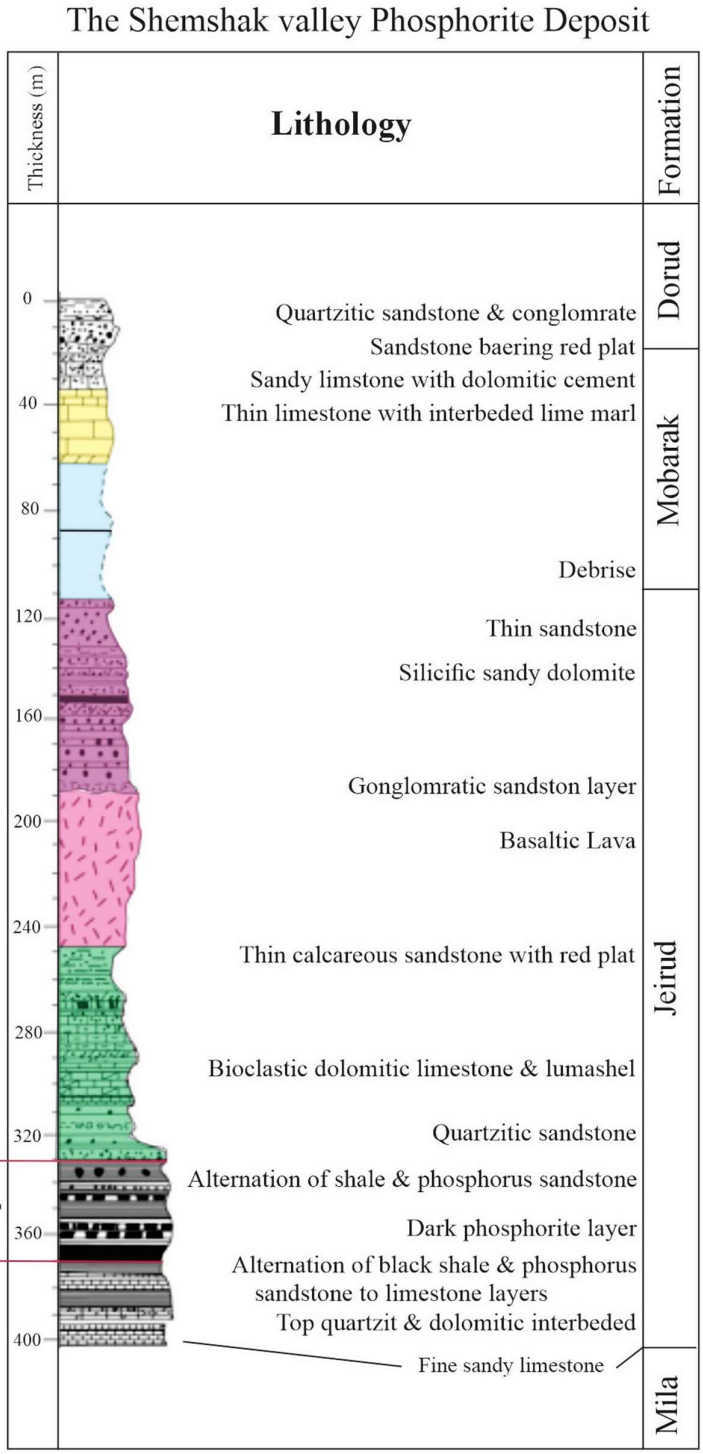

Figure 3. Stratigraphic section of the Jeirud Formation in the Alborz Magmatic Belt (Halalat & Bolourchi, 1994). Detailed stratigraphic log of the Shemshak Valley phosphorite deposit, showing the location of the collected phosphate samples

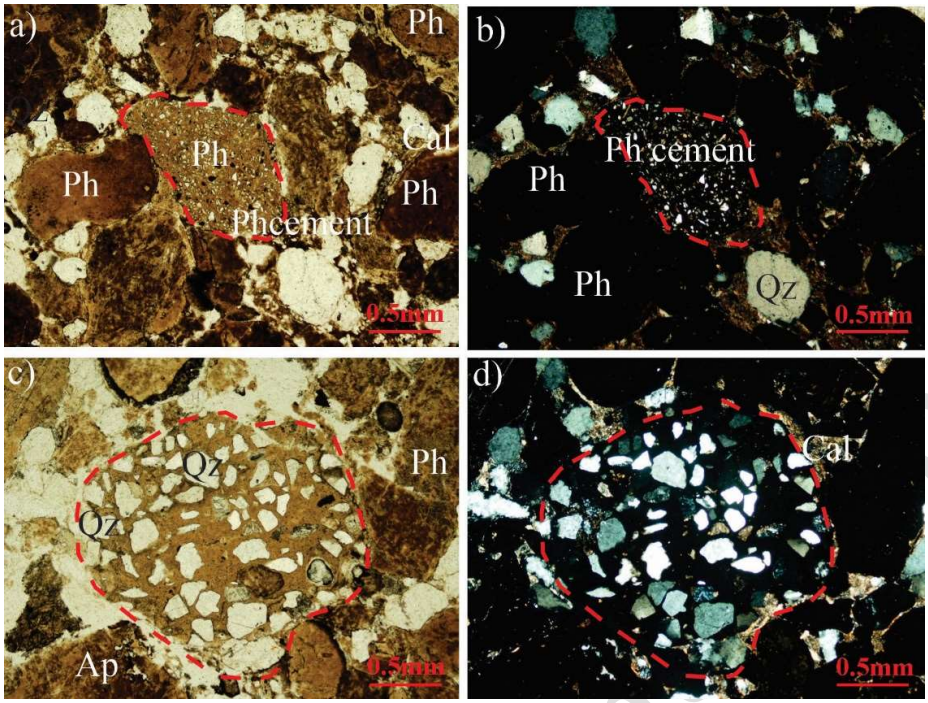

Figure 4. Photomicrographs of Jeirud phosphorite. a) Colony of phosphorite cementation (dashed line), various phosphorite pellets, quartz grains, and phosphate peloids partially replaced by Fe-oxides (PPL). b) Same view under XPL. c) Colony of phosphorite with pellets and quartz in the center; some phosphate peloids are replaced by Fe-oxides (PPL). d) Calcite cementation visible under XPL. Mineral abbreviations after Whitney & Evans, 2010 (Qz-quartz-; Ph-phosphorite; Ap- apatite; Cal-calcite)

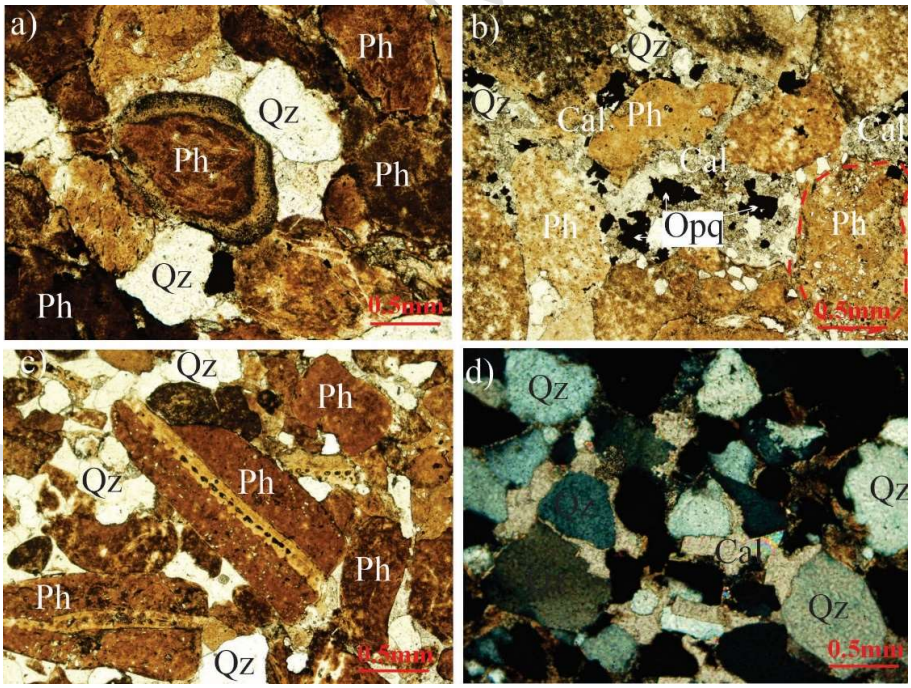

Figure 5. Photomicrographs of Jeirud phosphorite. a) Fine-grained phosphate peloid replaced by Fe-oxides in the center, with quartz grains and various phosphorite pellets (PPL). b) Phosphorite colony with opaque minerals and calcite cementation. c) Elongated phosphatic fragment with an oyster fragment and rounded quartz grain in a carbonate matrix, suggesting biogenic origin. d) Quartz and phosphorite pellets with calcite and dolomite cementation (XPL). Mineral abbreviations after Whitney & Evans, 2010 (Qz-quartz-; Ph-phosphorite; Opq- opaque minerals; Cal-calcite)

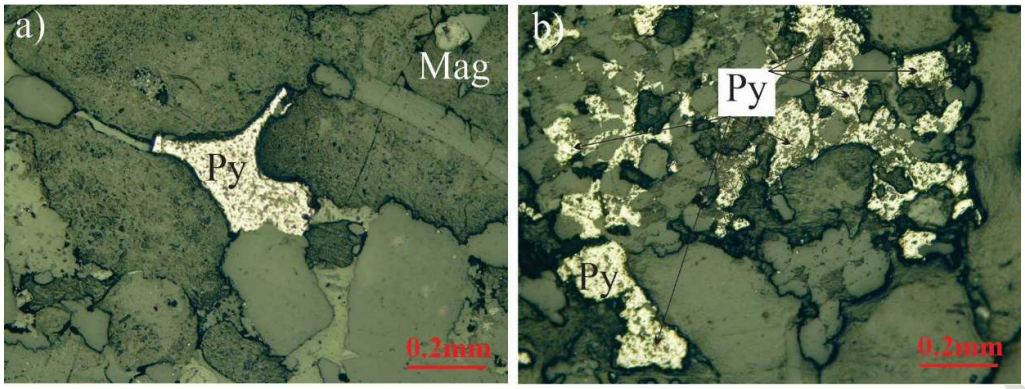

Figure 6. Reflected light photomicrographs. a, b) Pyrite and magnetite in polished section (PPL). (Mineral abbreviations after Whitney & Evans, 2010) (Py-pyrite; Mag-magnetite)

Phosphate clasts commonly contain bioclasts, including ostracod valves and bryozoan fragments, often partially replaced by collophane. An identified ostracod (Fig. 5c) provides biostratigraphic support for a Late Devonian age. Clay minerals (illite, kaolinite) are minor constituents (<10%) in sandy phosphorites but become dominant in shale-hosted varieties.
The overall mineralogy—dominance of fluorapatite (50–85%) and quartz (15–40%), with accessory carbonates (0–20%), sulfides (2–8%), and Fe-oxides—reflects deposition under low-energy, suboxic to anoxic conditions on a shallow marine shelf, with subsequent diagenetic overprinting.

Micro-XRF Elemental Mapping and Geochemistry

Major and Trace Element Distribution

High-resolution μ-XRF mapping of four thin sections provided detailed spatial data for elements from Na to U. Maps for P, Ca, and Si were fundamental for direct mineral identification (Figs. 7 and 8). High-intensity P areas correspond to fluorapatite. The Ca distribution strongly correlates with P in apatite but also reveals zones decoupled from P, indicating calcite ($CaCO_3$) (Fig. 8a–c). The Si map identifies the abundant quartz matrix and detrital grains.

Correlation of Fe and S maps confirmed the presence of pyrite (FeS_2) as euhedral to subhedral crystals (Fig. 8d, Fig. 9). Areas with high Fe but no S signal indicate iron oxides/hydroxides. The distribution of Ti, particularly when correlated with Ca and Si, is indicative of titanite ($CaTiSiO_5$) (Figs. 9b–d, 10, 11). Highly localized Zr signals correlating exclusively with Si confirm the presence of detrital zircon ($ZrSiO_4$) grains (Figs. 9d, 11a, b).

Sedimentary Textures and Diagenetic Alteration

The μ-XRF maps reveal that phosphates occur in two dominant morphologies: pelletal (oolitic) and peloidal forms (Figs. 7, 8). These rounded to subspherical aggregates support a primary sedimentary to early diagenetic origin in a low-energy, organic-rich marine setting (Glenn & Arthur, 1988; Glenn et al., 1994).

A key diagenetic feature is the partial to complete substitution of phosphate by iron oxides in specific zones (Figs. 10, 11). Areas originally rich in P show strong Fe signals with corresponding P depletion, indicating post-depositional oxidative replacement, forming secondary iron oxyhydroxides. This process is common in weathered phosphorites. The presence of Ti in some Fe-rich zones may indicate co-precipitation or alteration to stable Ti-bearing phases like titanite during this event.

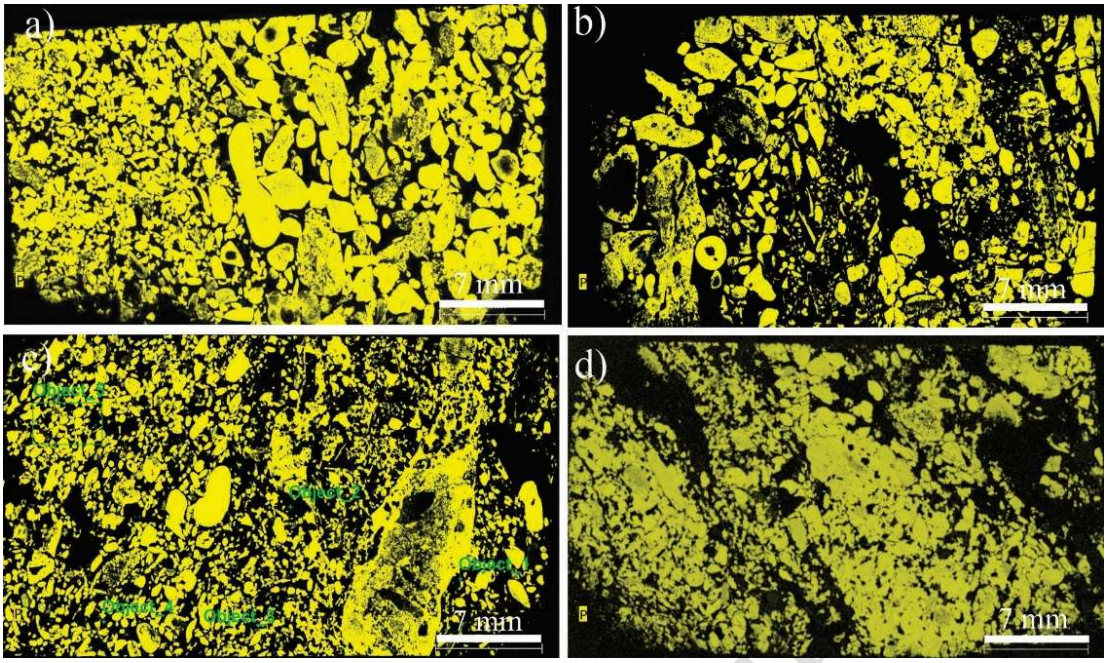

Figure 7. High-resolution μ-XRF elemental distribution maps showing phosphorus (P) concentration in four polished thin sections from the Jeirud Formation phosphorites. Color scales represent relative P counts (light yellow=low concentration; dark yellow=high concentration), with brighter colors indicating higher phosphorus content corresponding to fluorapatite. a) Sample JR01: Rounded to sub-rounded phosphate aggregates appear as discrete high-P domains (dark yellow) surrounded by lower-P matrix (light yellow), b) Sample JR02: Concentrically structured phosphate grains with high-P cores and variable marginal alteration are visible, c) Sample JR03: Large phosphate fragments with irregular shapes are present, d) Sample JR04: Lower P concentrations in the matrix correspond to quartz and/or carbonate cement, confirming the grain-supported nature of these phosphorites

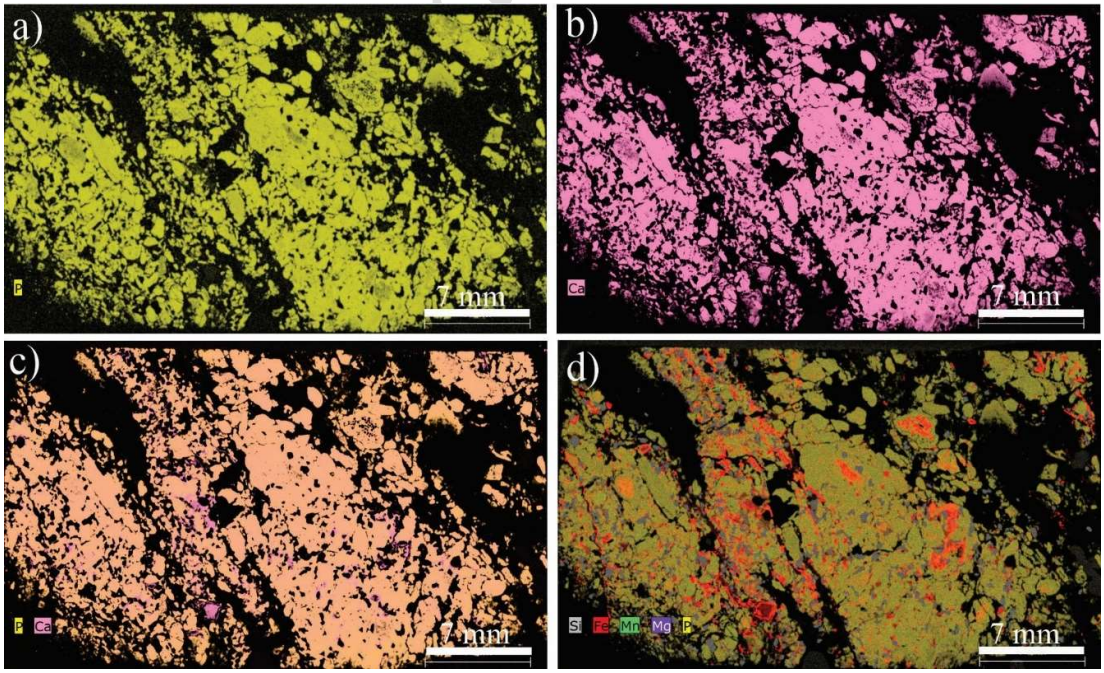

Figure 8. μ-XRF maps of sample JR04. a) Phosphorus (P) distribution. b) Calcium (Ca) distribution. c) Combined P and Ca map highlighting fluorapatite. d) Multi-element map (Si, Fe, Mn, Mg, P) showing mineral associations and sedimentary textures

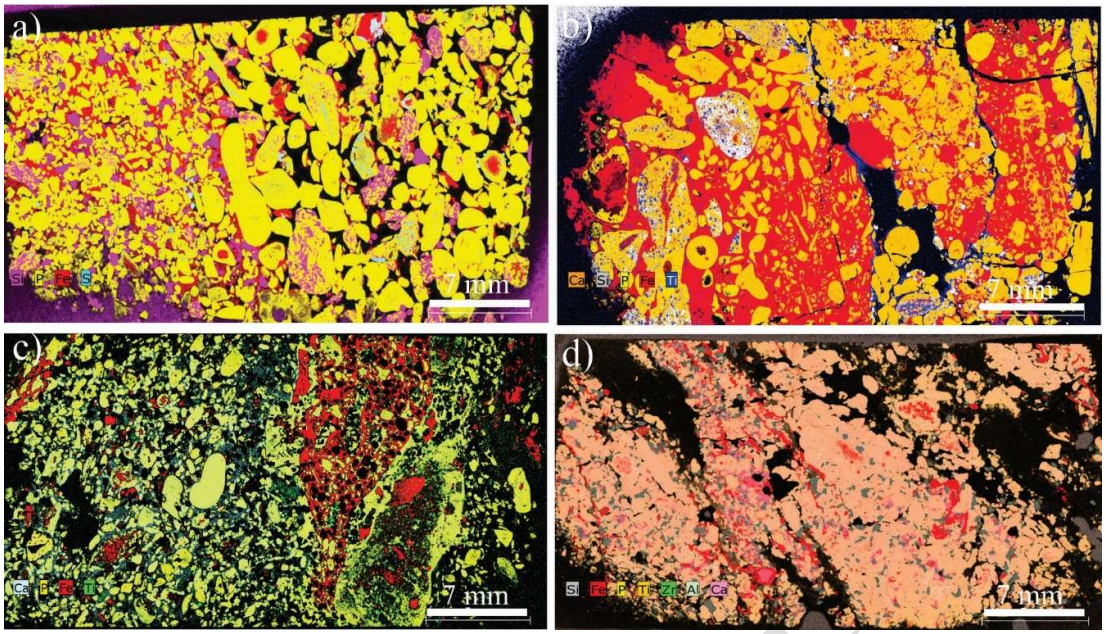

Figure 9. Multi-element μ-XRF maps of a phosphate thin section. a) Distribution of P, Si, Fe, and S, showing pyrite (Fe-S correlation) and fluorapatite (P-rich areas) (sample JR01). b) Distribution of P, Ca, Si, Fe, and Ti, highlighting titanite (Ca-Ti-Si association) (sample JR02). c) Distribution of P, Ca, Fe, and Ti, highlighting zones of potential Fe substitution (sample JR03). d) Distribution of P, Ca, Si, Fe, Ti, Al, and Zr, indicating zircon (Zr-Si correlation) and the siliciclastic matrix (sample JR04)

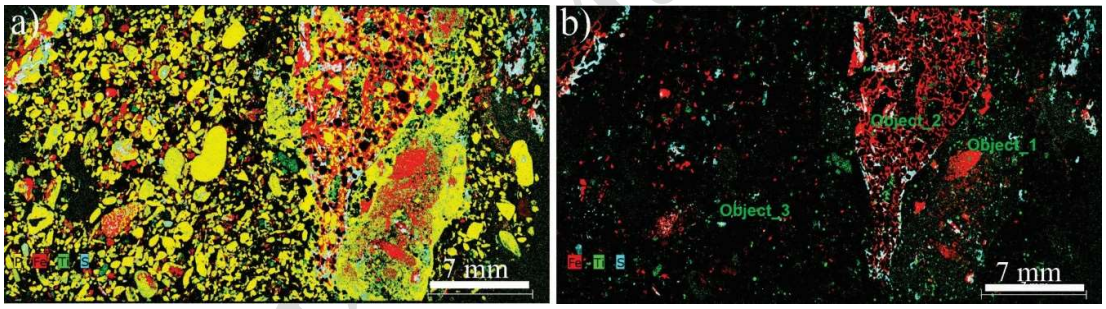

Figure 10. μ-XRF maps of sample JR03. a) Distribution of P, Fe, Ti, and S, showing zones where Fe signal replaces P (diagenetic alteration) and sulfur minerals such as pyrite. b) Fe, Ti, and S associations, indicating pyrite and Ti-bearing phases (e.g., titanite) in altered zones

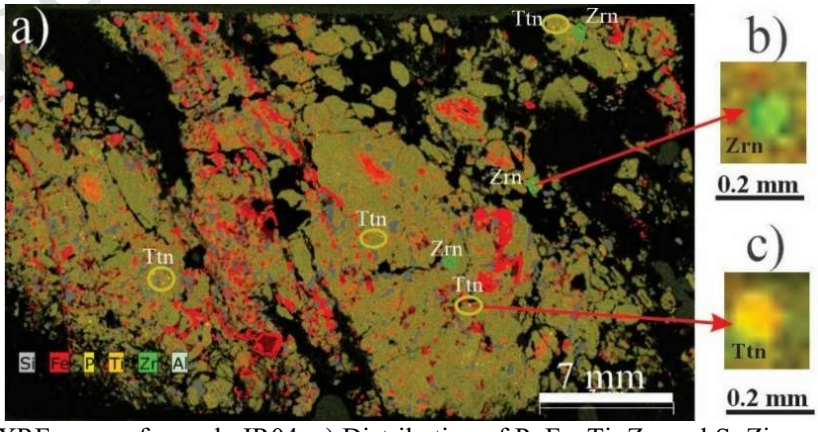

Figure 11. μ-XRF maps of sample JR04. a) Distribution of P, Fe, Ti, Zr, and S. Zircon (Zr-Si) grains are identified. b) Ti-rich zones suggesting titanite ($CaTiSiO_5$) presence, often associated with Fe-rich altered phosphates. (Mineral abbreviations after Whitney & Evans, 2010)

Rare Earth Element (REE) Geochemistry

Quantitative spot μ-XRF analysis revealed significant trace element concentrations, including Sr and U. Rare earth elements were notably enriched within the fluorapatite phase, showing a positive correlation with P and Ca, indicative of substitution for Ca in the apatite lattice-a characteristic of sedimentary phosphorites.

Total REE (ΣREE) concentrations were variable but significant, consistent with reported values of ~370–800 ppm for Jeirud phosphorites (Moghaddasi, 2017). Chondrite-normalized REE patterns exhibit light REE (LREE) enrichment over heavy REE (HREE) and no pronounced Ce anomaly. This pattern is consistent with suboxic to anoxic depositional conditions, where reducing environments prevented significant Ce fractionation during apatite precipitation. Trace amounts of zircon were identified as secondary REE hosts (Fig. 11a).

Discussion

The formation of sedimentary phosphorites in Iran is intrinsically linked to the tectonic evolution of the Proto-, Paleo-, and Neo-Tethys oceans (Maghfouri et al., 2019, 2020; Movahednia et al., 2022; Hashempour et al., 2024). The Upper Devonian Jeirud Formation correlates temporally with the Paleo-Tethys Ocean. Iranian phosphorites predominantly occur along paleo-passive margins, with the Alborz Magmatic Belt hosting over 80% of known deposits (Hashempour et al., 2024).

The pelletal and peloidal textures observed via μ-XRF are diagnostic of sedimentary phosphogenesis in organic-rich shelf settings under fluctuating redox conditions. Their preservation suggests limited physical reworking. The detection of detrital zircon provides constraints on sediment provenance, while authigenic/diagenetic titanite points to post-depositional fluid activity.

However, the widespread iron substitution observed in multiple samples (Figs. 10, 11) signifies significant post-depositional oxidative diagenesis, likely during later uplift or exposure. This alteration can mobilize phosphorus and modify REE patterns, though the core geochemical signature (LREE enrichment, lack of Ce anomaly) appears preserved. The coexistence of primary sedimentary textures with secondary Fe–Ti alteration underscores the complex, multi-stage history of the Jeirud phosphorites.

A systematic comparison between quantitative μ-XRF and ICP-OES data from identical samples reveals a strong correlation for major and minor element concentrations. This validates μ-XRF as an accurate and reliable non-destructive technique. Its principal advantages are rapid, cost-effective analysis without complex sample preparation and the capacity for high-resolution spatial mapping. Consequently, μ-XRF is a powerful tool for quantitative and qualitative geochemical assessment, aiding in provenance and diagenetic studies, as well as in evaluating the economic potential of phosphate deposits. This validation demonstrates that μ-XRF data can effectively complement or, in many applications, replace conventional destructive methods like ICP-OES, with the added benefit of preserving sample integrity.

Conclusions

High-resolution μ-XRF analysis effectively characterized the mineralogy and diagenetic history of the Jeirud Formation phosphorites, confirming fluorapatite as the dominant phase and identifying accessory pyrite, iron oxides, titanite, and zircon. The technique clearly revealed primary sedimentary (peloidal) textures and secondary oxidative diagenetic processes, notably the replacement of phosphate by iron oxides. Quantitative spot analysis confirmed REE enrichment within the fluorapatite, with patterns indicative of suboxic to anoxic depositional

conditions. A strong correlation between μ-XRF and bulk ICP-OES data supports μ-XRF as a reliable, non-destructive method for initial, high-resolution geochemical characterization and elemental mapping of phosphates. However, μ-XRF should be viewed as complementary to, not a full substitute for, ICP-OES/MS when precise quantification particularly for trace elements and REEs near detection limits is required. For follow-up, employ ICP-OES/MS to achieve high-precision trace and REE measurements, especially at low concentrations.

Acknowledgments

We extend our sincere gratitude to Fazilat Yousefi at the University of New Brunswick for her expert technical support and assistance during the μ-XRF analyses. Financial support for this work was provided by an NSERC Discovery Grant to David R. Lentz and by the Vice Chancellor for Research at Payame Noor University, which funded field sampling and sample preparation. We also wish to thank the anonymous reviewers and the editorial team for their insightful and constructive comments, which greatly improved the clarity and quality of the manuscript.

Authors' Contributions

Mahboobeh Jamshidibadr: Investigation (sampling), Formal analysis, Writing – original draft, Writing – review & editing.

Seyed Javad Moghaddasi: Investigation (sampling), Investigation (field activities), Writing – review & editing.

David Richard Lentz: Formal analysis, Validation, review.

Conflicts of interest

The authors declare no conflicts of interest.

References

Abed, A.M., 2013. The eastern Mediterranean phosphorite giants: an interplay between tectonics and upwelling. GeoArabia 18: 67-94.

Abed, A.M., Jaber, O., Alkuisi, M., Sadagah, R., 2016. Rare earth elements and uranium geochemistry in the Al-Kora phosphorite province, Late Cretaceous, northwestern Jordan. Arabian Journal of Geosciences 9: 187. https://doi.org/10.1007/s12517-015-2135-6

Aghanabati, A., 1998. Major sedimentary and structural units of Iran (map). Geosciences Scientific Quarterly Journal 7: 29-30.

Aghanabati, A., 2004. Geology of Iran. Geological Survey and Mineral Exploration of Iran, 582 pp. (in Persian).

Alavi, M., 1996. Tectonostratigraphic synthesis and structural style of the Alborz mountain system in Northern Iran. Journal of Geodynamics 21: 1-33.

Assereto, R., 1966. Explanatory notes on geological map of upper Djadjerud and Lar valleys (central Elburz, Iran), scale 1:50,000. Instituto di Geologia dell, Universita di Milano, Serie G, Pubblicazione 232: 1-86.

Avini, M., 1987. Unpublished report on the preliminary technical and economical studies of the Jeirud phosphate deposit; detailed exploration project on phosphate occurrences within the Jeirud, Soltanieh, and Zagros formations. National Iranian Steel Company, 108 p.

Banerjee, S., Choudhury, T.R., Saraswati, P.K., Khanolkar, S., 2020. The formation of authigenic deposits during Paleogene warm climatic intervals: a review. Journal of Palaeogeography 9: 1-27. https://doi.org/10.1186/s42501-020-00076-8

Boggs, S., 2009. Petrology of Sedimentary Rocks (2nd ed.). Cambridge University Press, 600 pp.

Cook, P.J., Banerjee, D.M., Southgate, P.N., 1990. The phosphorus resources of Asia and Oceania. In:

Phosphorus Requirements for Sustainable Agriculture in Asia and Oceania, International Rice Research Institute, Los Baños, pp. 97-114.
Daryin, A.V., Baryshev, V.B., Zolotarev, K.V., 1991. Scanning X-ray fluorescence microanalysis of phosphorites from the underwater mountains of the Pacific. Nuclear Instruments and Methods in Physics Research Section A: Accelerators, Spectrometers, Detectors and Associated Equipment 308: 318-320.
Flude, S., Haschke, M., Storey, M., 2017. Application of benchtop micro-XRF to geological materials. Mineralogical Magazine 81: 923-948.
Föllmi, K.B., 1996. The phosphorus cycle, phosphogenesis and marine phosphate-rich deposits. Earth-Science Reviews 40: 55-124.
Ernst, A., Mohammadi, M., 2009. Stenolaemate bryozoans from the Geirud Formation (Upper Devonian/Lower Carboniferous) of Central Alborz (Iran). Paläontologische Zeitschrift 83: 439-447.
Garnit, H., Bouhlel, S., Barca, D., Chtara, C., 2012. Application of LA-ICP-MS to sedimentary phosphatic particles from Tunisian phosphorite deposits: insights from trace elements and REE into paleo-depositional environments. Chemie der Erde Geochemistry 72: 127-139.
Garnit, H., Bouhlel, S., Jarvis, I., 2017. Geochemistry and depositional environments of Paleocene-Eocene phosphorites: Metlaoui Group, Tunisia. Journal of African Earth Sciences 134: 704-736.
Ghavidel-Syooki, M., 1995. Palynostratigraphy and palaeogeography of a Palaeozoic sequence in the Hassanakdar area, Central Alborz Range, northern Iran. Review of Palaeobotany and Palynology 86: 91-109.
Glenn, C.R., Arthur, M.A., 1988. Petrology and major element geochemistry of Peru margin phosphorites and associated diagenetic minerals: authigenesis in modern organic rich sediments. Marine Geology 80: 231-268.
Glenn, C.R., Föllmi, K.B., Riggs, S.R., Baturin, G.N., Grimm, K.A., Trappe, J., Abed, A.M., Galli-Oliver, C., Garrison, R.E., Ilyin, A.V., Jehl, C., Rohrlich, V., Sadaqah, R.M.Y., Schidlowski, M., Sheldon, R.E., Siegmund, H., 1994. Phosphorus and phosphorites: sedimentology and environments of formation. Eclogae Geologicae Helvetiae 87(3): 747-788.
Haghipour, A., Zhakiipur, A., Taraz, H., Vahedeni, F., 1986. Tehran Quadrangle Geological Map, Scale 1:250,000. National Organization for Geology and Mineral Exploration, Tehran.
Halalat, H., Bolourchi, M., 1994. Geology of Iran: Phosphate. Geological Survey of Iran, Tehran, 362 pp. (in Persian with English abstract)
Hashempour, S.S., Maghfouri, S., Rastad, E., González, F.J., 2024. Metallogeny and Temporal-Spatial Distribution of Sedimentary Phosphorite Mineralization in Iran, Relation to Tethyan Oceans Evolution and Implications for Future Exploration. Ore Geology Reviews 164: 105855. https://doi.org/10.1016/j.oregeorev.2023.105855
Heidarian, H., Lentz, D.R., Thorne, K., Rogers, N., 2021. Application of portable X-ray and micro-X-ray fluorescence spectrometry to characterize alteration and mineralization within various gold deposits hosted in southern New Brunswick, Canada. Journal of Geochemical Exploration 229: 106847. https://doi.org/10.1016/j.gexplo.2021.106847
Jasinski, S.M., 2011. Phosphate rock. In: Mineral Commodity Summaries 2011, United States Geological Survey, United States Government Printing Office, Washington, D.C., pp. 118-119.
Jasinski, S.M., 2016. Mineral commodity summaries 2016: Phosphate rock. U.S. Geological Survey, pp. 124-125.
Kechiched, R., Laouar, R., Bruguier, O., Salmi-Laouar, S., 2020. A comprehensive review on the Upper Cretaceous-Eocene phosphorites of the Tebessa region (eastern Algeria): Implications for genesis and exploration. Journal of African Earth Sciences 162: 103708.
Kocsis, L., Gheerbrant, E., Mouflih, M., Cappetta, H., Ulianov, A., Chiaradia, M., Bardet, N., 2014. Comprehensive stable isotope investigation of marine biogenic apatite from the late Cretaceous-early Eocene phosphate series of Morocco. Palaeogeography, Palaeoclimatology, Palaeoecology 394: 74-88.
Kocsis, L., Gheerbrant, E., Mouflih, M., Cappetta, H., Yans, J., Amaghzaz, M., 2016. Gradual changes in upwelled seawater conditions (redox, pH) from the late Cretaceous through early Paleogene at the northwest coast of Africa: negative Ce anomaly trend recorded in fossil bio-apatite. Chemical Geology 421: 44-54.
Lucas, J., Prévôt-Lucas, L., 1995. Tethyan phosphates and biogenic sediments: A genetic model. In:

Notholt, A.J.G., Jarvis, I. (Eds.), Phosphate Deposits of the World, vol. 2. Cambridge University Press, Cambridge, pp. 5-34.
Maghfouri, S., Rastad, E., Borg, G., Hosseinzadeh, M.R., Movahednia, M., Mahdavi, A., Mousivand, F., 2020. Metallogeny and temporal-spatial distribution of sediment hosted stratabound copper (SSC-type) deposits in Iran; implications for future exploration. Ore Geology Reviews 127: 103834.
Maghfouri, S., Rastad, E., Movahednia, M., Lentz, D.R., Hosseinzadeh, M.R., Ye, L., Mousivand, F., 2019. Metallogeny and temporal-spatial distribution of manganese mineralizations in Iran: implications for future exploration. Ore Geology Reviews 115: 103026.
Moghaddasi, S.J., 2017. Mineralogy and Rare Earth Elements Geochemistry of Jeirud Phosphate Deposit in Shemshak Valley, North Tehran. Geosciences 26: 313-324. (in Persian with English abstract)
Movahednia, M., Maghfouri, S., Fazli, N., Rastad, E., Ghaderi, M., González, F.J., 2022. Metallogeny of Manto-type stratabound Cu-(Ag) mineralization in Iran: Relationship with NeoTethyan evolution and implications for future exploration. Ore Geology Reviews 149: 105064.
Namdmalian, E., Akhot, Z., Momenzadeh, M., 1998. Phosphate in Iran. National Organization for Geology and Mineral Exploration, Tehran, 189 pp. (in Persian).
Notholt, A.J.G., Sheldon, R.P., Davidson, D.F. (Eds.), 1989. Phosphate Deposits of the World: Volume 2, Phosphate Rock Resources. Cambridge University Press, Cambridge, 566 pp.
Orris, G.J., Chernoff, C.B., 2004. Data set of world phosphate mines, deposits, and occurrences. U.S. Geological Survey Open-File Report 2004-1006, 61 pp.
Pufahl, P.K., Grimm, K.G., Abed, A.M., Sadaqah, R.M.Y., 2003. Upper Cretaceous (Campanian) phosphorites in Jordan: implications for the formation of a south Tethyan phosphorite giant. Sedimentary Geology 161: 175-205.
Pufahl, P.K., Groat, L.A., 2016. Sedimentary and igneous phosphate deposits: formation and exploration: an invited paper. Economic Geology 112: 483-516.
Shanahan, T.M., Overpeck, J.T., Hubeny, J.B., King, J., 2008. Scanning micro-X-ray fluorescence elemental mapping: A new tool for the study of laminated sediment records. Geochemistry, Geophysics, Geosystems 9. https://doi.org/10.1029/2007GC001800
Tzifas, I.T., Godelitsas, A., Magganas, A., Anderoulakash, E., Eleftherioud, G., Merizimckis, T.J., Perraki, M., 2014. Uranium-bearing phosphatized limestone of new Greece. Journal of Geochemical Exploration 143: 62-137.
Van Kauwenbergh, S.J., 2010. World phosphate rock reserves and resources. International Fertilizer Development Center (IFDC), Technical Bulletin no. 75, Muscle Shoals, Alabama, USA, 58 pp.
Wendt, J., Kaufmann, B., Belka, Z., Farsan, N., Karimi Bavandpour, A., 2005. Devonian/Lower Carboniferous stratigraphy, facies patterns and palaeogeography of Iran Part II. Northern and central Iran. Acta Geologica Polonica 55 (1): 31-97.
Whitney, D.L., Evans, B.W., 2010. Abbreviations for names of rock-forming minerals. American Mineralogist 95(1): 185-187.
Zilkey, D.R., Baud, A., Francus, P., Antoniades, D., Gregory-Eaves, I., 2024. A pan-Canadian calibration of micro-X-ray fluorescence core scanning data for prediction of sediment elemental concentrations. Environmental Advances 15: 100495. https://doi.org/10.1016/j.envadv.2024.100495